Computational Scaling Relationships Predict Experimental Activity and Rate Limiting Behavior in Homogenous Water Oxidation

Daniel R. Harper[1,2] and Heather J. Kulik[1,]*

[1]*Department of Chemical Engineering, Massachusetts Institute of Technology, Cambridge, MA 02139*

[2]*Department of Chemistry, Massachusetts Institute of Technology, Cambridge, MA 02139*

ABSTRACT: While computational screening with first-principles density functional theory (DFT) is essential for evaluating mechanisms of candidate catalysts, limitations in accuracy typically prevent prediction of experimentally relevant activities. Exemplary of these challenges are homogeneous water oxidation catalysts (WOCs) where differences in experimental conditions along with small changes in ligand structure can alter rate constants by over an order of magnitude. To leverage computational screening for homogeneous WOC design, a distinct approach is needed. Here, we compute mechanistically-relevant electronic and energetic properties for 19 mononuclear Ru transition metal complexes (TMCs) from three experimental water oxidation catalysis studies. We discover that 15 of these TMCs have experimental activities that can be correlated to a single property, the ionization potential of the Ru(II)-O_2 catalytic intermediate. This scaling parameter is well correlated with experimentally-reported rate constants, allowing quantitative understanding activity trends and insight into rate-limiting behavior. We use this approach to rationalize differences in activity with differing experimental conditions, and we qualitatively analyze the source of distinct behavior for differing electronic states in the other four catalysts. Comparison to closely related single-atom catalysts and modified WOCs enables rationalization of the source of rate enhancement in these experimental WOC catalysts.

1. Introduction.

Improved catalysts are essential for renewable energy, for instance in the water oxidation reaction to enable production of renewable solar fuels.[1] Homogeneous catalysts have attracted significant interest as water oxidation catalysts (WOCs) for this reaction because the properties of transition metal complexes (TMCs) can be finely tuned though ligand modification.[2-4] Water oxidation has been demonstrated at a single metal site TMC[5-6], motivating efforts to optimize these WOCs. Experimental efforts to determine the ligands compatible with water oxidation[7-9] or identify design criteria for more active WOCs[10-14] often consist of trial-and-error synthesis of a set of TMCs and measurement of their activity.[7-14] This approach has led to significantly improved homogeneous WOCs, the most active of which contain Ru metal centers.[15-16] However, many of these improved catalysts rely on through-space interactions[16-19] such as pendant bases[18-19] to achieve an increase in catalytic activity. Ligand modifications that instead improve catalytic activity via through-bond effects are desirable since they are more robust to changes in reaction conditions and provide a complementary approach to further increasing activity. Rational WOC design would benefit from first-principles modeling, but subtle changes in activity that also depend on experimental conditions can be challenging to predict *a priori*.

A number of mechanisms for water oxidation have been proposed. We focus on the water nucleophilic attack (WNA)[20] mechanism which is thought to be responsible for the most active catalyst identified thus far[16] (Scheme 1). Although there is strong support for the WNA mechanism, water oxidation is also believed to be possible via the dimerization of two metal-oxo units.[21-23] Experimental methods are capable of providing insight regarding specific details of this mechanism,[24-26] but accurate computational modeling is expected to be critical to gain a more complete understanding of the intermediates and competing pathways.[27] The WNA

mechanism has been characterized computationally,[28-29] with particular emphasis on the electronic structure and reactivity of the high-valent Ru(V)=O species,[30-32] the O_2 release step,[33] and photoisomerization.[34] However, it is not yet known which fundamental properties predict catalytic activity, a key piece of information for computationally-guided design for homogeneous WOCs.

Scheme 1. The water nucleophilic attack (WNA) mechanism for water oxidation. Steps are colored based on the type of each reaction. Oxygen dissociation is shown in blue. Proton coupled electron transfer steps (PCET) are shown in black. Electron transfer steps are colored yellow. The "key" O-O bond formation step is shown in green.
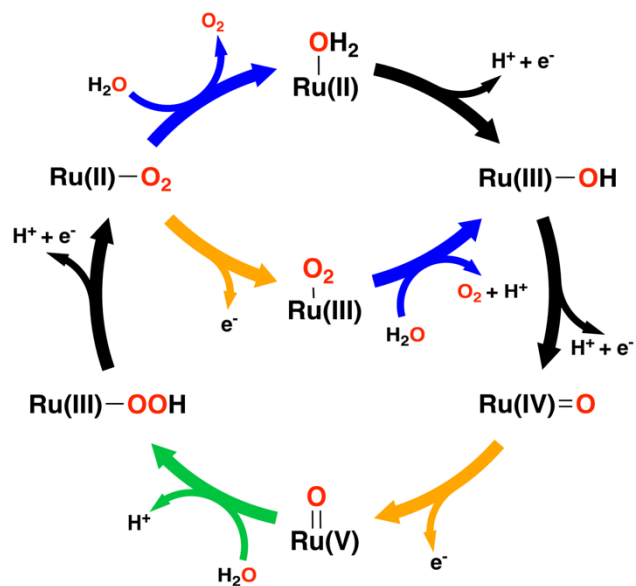

Computation is an effective tool for accelerating the discovery of novel catalysts,[35-36] but it is necessary to accurately obtain properties which correlate to experimentally measured catalytic activity since direct prediction of experimental rates can be challenging. A focus on a single scaling parameter for WOCs is motivated by the fact that many ligand modifications which result in more active WOCs are thought to function by modifying the rate determining step in the WNA mechanism.[37-41] These ligand designs have included oxygen atom transfer to a pendant base,[38] nucleophilic attack by a carboxylate group,[39-40] and additional elementary steps

related to reversible changes in ligand conformation.[41] The flexibility of the precise rate-determining steps within the WNA framework is typical of homogeneous catalysis[42-44] and computation has been essential in identifying this variability.[45-47] While changes in mechanism and catalytic activity can be quantified directly through microkinetic modelling[48] or through formalisms such as the degree of rate control[49-50] or the energetic span model[51-52], prediction of experimental rates remains challenging. The close association between ligand modification, mechanistic changes, and catalytic activity further motivates that idea that scaling relationships in homogeneous catalysis should be tailored for subsets of closely-related TMCs to predict their experimental activities directly.

While more frequently exploited in heterogeneous catalysis[53-55], catalyst screening can be simplified by identifying linear correlations (i.e. scaling relationships), an approach which has been demonstrated fruitfully on related metal-organic frameworks,[56-57] single-atom catalysts,[58-59] and homogeneous systems.[60-62] Further, scaling relationships predict the relative activity of catalysts, which provides the added benefit of cancelling some of the systematic error[63] present in density functional theory (DFT)[64-68] and particularly in TMCs.[64, 69-71] While universal scaling relationships for WOCs have been proposed,[72-73] recent work (e.g., in C–H activation) suggests[74-77] that scaling relationships in homogeneous catalysis need to be tailored for specific ligand types[78] and should account for the influence of reaction conditions.[44]

In this work, we compare the computed properties of homogeneous WOCs to previously reported rate constants on closely related WOCs from three different experimental studies (Figure 1 and Supporting Information Table S1).[8, 12-14] To demonstrate the utility of scaling relationships for reducing errors in computational catalyst screening, we select only WOCs which are thought to be active via the WNA mechanism, avoid though-space interactions with

the catalytic intermediate, and contain a ruthenium metal center. For the 19 homogeneous catalysts that fit these criteria, we propose a metric for identifying similar and dissimilar electronic states. We demonstrate that effective scaling relationships can be constructed for catalysts with similar electronic states, but that these do not readily extend to all WOCs. We show that our scaling parameter accurately predicts the relative activity of catalysts within these closely-related TMCs and that different slopes in these scaling relations prevail when experimental conditions are varied.
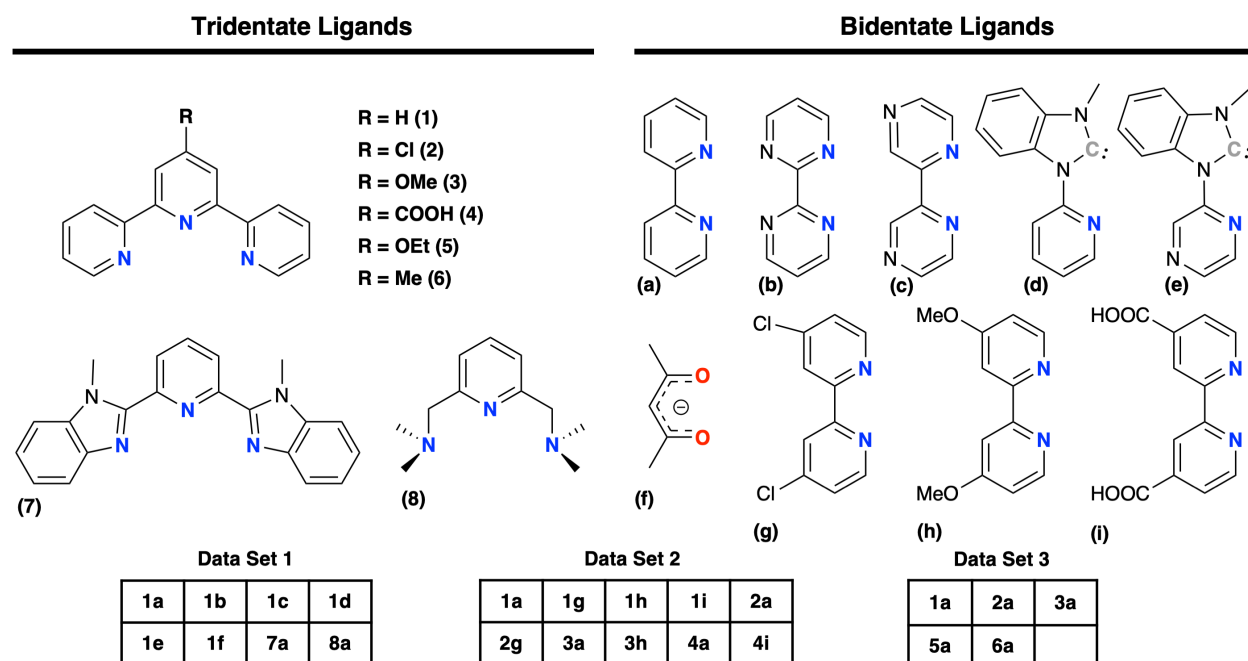
Figure 1. The 19 TMCs considered in this work from three literature sources, data sets 1[8], 2[12], and 3[13-14]. Each TMC consists of a ruthenium metal center compelxed with a tridentate ligand (left) and a bidentate ligand (right). Experimentally measured rate constants for the water oxidation reaction are available for each TMC, from at least one of three literature sources, as indicated in the grid at bottom.

2. Computational Details

All geometry optimizations and single-point calculations were performed using density functional theory (DFT) and a developer version of TeraChem v1.9.[79-80] The B3LYP[81-83]

5

functional was employed with the LANL2DZ[84] effective core potential for Ru and the 6-31G*

basis set[85] for all elements. Solvent corrections, ΔG_{solv}, were added using the conductor-like

polarizable continuum implicit solvent model[86-87] implemented[88-89] in TeraChem with a dielectric

constant of 80. Singlet calculations were carried out in a spin-restricted formalism, while all

other calculations were spin unrestricted, and the lowest energy spin multiplicity was always

reported for each intermediate (Supporting Information Table S2 and Figure S1). Level shifting

was applied with the virtual orbitals shifted by 0.25 Ha.[90] Geometry optimization in translation

rotation internal coordinates[91] using the L-BFGS algorithm were carried out on molecules in

implicit solvent. Default geometry optimization convergence thresholds of 4.5 x 10^{-4} Ha/bohr

and 10^{-6} Ha were used for the gradient and change in the total energy between steps,

respectively. For each optimized geometry, we computed the Hessian to confirm the absence of

any imaginary frequencies and to obtain energy corrections for the zero point energy and entropy

at a temperature of 300 K. Entropic terms from other (i.e., rotational, translational, and entropic)

degrees of freedom were neglected. Population analysis was carried out with an interface

between TeraChem and Natural bonding orbital analysis (NBO) v6.0.[2]

Initial structures for each unique TMC and each intermediate of the WNA catalytic cycle

were either generated using molSimplify[92-94] which uses OpenBabel[95-96] as a backend or by

modifying a previously converged structure (Supporting Information Table S3). As in prior

work, the successful completion of each calculation was judged based on two criteria.[97] First, the

final structure was required to pass a series of geometric health checks to ensure that the

calculation converged to the desired octahedral geometry (Supporting Information Table S4). For

all open-shell calculations, the deviation from the expected value of $<S^2>$ (i.e., $S(S+1)$) was

required to be less than a 1 μ_B^2 heuristic cutoff for spin contamination (Supporting Information

Table S5).

In this work, we developed strategies to recover jobs that failed to pass the $\langle S^2 \rangle$ check or for which the self-consistent field (SCF) calculation failed to converge. For spin-contaminated cases, the geometry optimization was attempted with the fraction of Hartree-Fock (HF) exchange set to 0% (i.e. BLYP). For cases with SCF failures, level-shifting values were adjusted to 1.0 Ha for the majority spin virtual orbitals and 0.1 Ha for the minority spin virtual orbitals. When these recovery strategies were successful in addressing the original failure, their final structures and wavefunctions were used as inputs to a new geometry optimization using the B3LYP (i.e., 20% HF) functional and the original level shift values of 0.25 Ha (Supporting Information Table S6).

To validate our choice of DFT functional, we compared results to B3LYP with modified amounts of HF exchange (i.e., (0-30% in increments of 5%) and three range-separated hybrid functionals, CAM-B3LYP,[98] ωB97X,[99] and LRC-ωPBEh[100] (Supporting Information Text S1). We observed the linear correlation between computed free energy values and experimentally-measured benchmarks to be insensitive to functional choice, with the linear correlation comparable (R^2: 0.84–0.90) regardless of the functional selected (Supporting Information Figure S2).

Three types of properties were calculated in order to capture trends in the WNA mechanism that could predict the overall rates of the experimentally measured catalytic cycle. We calculated the free energy of reaction, ΔG, at pH = 0 and 300 K for each step while incorporating corrections for zero-point vibrational energy, entropy, and the solvation environment. The energetics of the rigid ligand dissociation energy, ΔE_{LD}, of oxygen from the Ru(II)-O$_2$ and Ru(III)-O$_2$ intermediates as well as the vertical ionization potential, ΔE_{IP}, of the Ru(II)-O$_2$ and Ru(IV)=O intermediates were determined based on single point calculations

(Supporting Information Text S2). The calculation of ΔE_{LD} and ΔE_{IP} neglected the corrections for zero-point vibrational energy and entropy. This approximation was motivated by the nearly constant (std. dev. < 1 kcal/mol) value of these corrections in the computation of ΔE_{LD} (Supporting Information Table S7).

3. Results and Discussion.

3a. Energetics of a Representative WOC.

We first focus on TMC **1a**, a well-known WOC[5, 8, 12-14, 20, 29-30, 33] that can be used to quantify baseline reaction energetics (Figure 1). As **1a** was among the first mononuclear WOCs discovered[5], it is included in all of the experimental data sets considered in this work and is expected to be broadly representative of TMCs that catalyze the WNA mechanism (Scheme 1). The **1a** structure also contains motifs common among most of the catalysts in this work (Figure 1). Specifically, the **1a** structure has an octahedral coordination geometry with nitrogen atoms from tridentate and bidentate ligands that coordinate the metal in a geometry that constrains ligating atom positions (Figure 1). The WNA mechanism that **1a** participates in is believed to include three proton-coupled electron transfer (PCET) steps,[101] two electron transfer steps, two O_2 dissociation step, and an O-O bond formation step, which can each have different degrees of control over overall catalytic activity (Scheme 1).

To determine potential rate limiting steps in the WNA catalytic cycle, we computed the reaction coordinate for TMC **1a** (Figure 2). For each PCET step, the reaction is exothermic when we account for an oxidant with a redox potential of 1.6 V,[102] suggesting these steps are unlikely to be rate limiting. In comparison, the other two electron transfer steps, Ru(IV)=O to Ru(V)=O and Ru(II)-O_2 to Ru(III)-O_2, require 0.67 eV and 0.15 eV, respectively, even after accounting for an oxidant (Supporting Information Table S8). For the two O_2 dissociation steps, we note that

each is included in a different possible reaction pathway (Scheme 1). Since the dominant

pathway is influenced by the rate of electron transfer from Ru(II)-O_2, either O_2 dissociation step

has the possibility of being rate limiting. Finally, the O-O bond formation step is strongly

exothermic (i.e., ΔG = -1.06 eV), but this thermodynamic favorability does not guarantee

favorable kinetics *a priori* (Supporting Information Table S8). After eliminating the three PCET

steps as candidate rate-limiting steps based on our calculations, the remaining options, i.e., two

electron transfer steps, the O-O bond formation step, and two O_2 dissociation steps, are

consistent with those that have been identified as rate limiting in experimental studies.[8, 14, 20, 30]
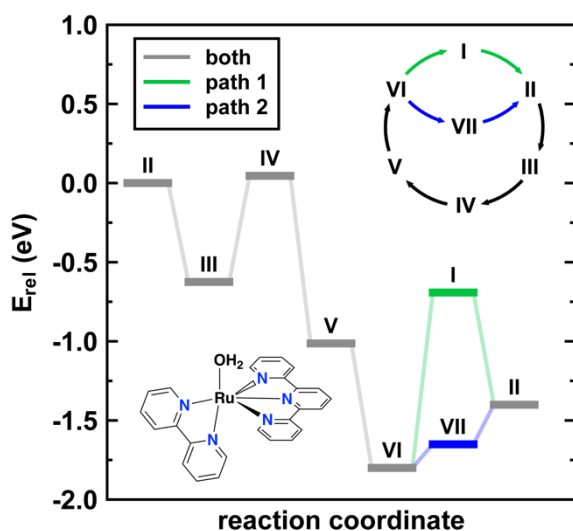

Figure 2. Energetics of the WNA catalytic cycle for TMC **1a**. The labeling of intermediates is inset (top right) and corresponds to the catalytic cycle shown in Scheme 1. For steps involving the transfer of an electron (I to II, II to III, III to IV, V to VI, and VI to VII), we add -1.6 eV to the step's energetics to account for the presence of an external oxidant. Energetics are shown for both the reaction path where O_2 directly dissociates (green) and the path where an electron transfer precedes O_2 dissociation (blue). For most intermediates, the two paths are identical (gray).

To aid interpretation and accelerate screening, we identify electronic properties that we

can easily compute with DFT but are still related to each of the five candidate rate limiting steps,

and thus could correlate with the overall experimentally-measured reaction rate. To avoid

explicit calculation of time-consuming transition states, we rely on the Bell-Evans-Polanyi (BEP)

principle[103-104] and compute quantities related to reaction free energies, ΔG. Thus, to model the rate of O-O bond formation or electron transfer steps, we use the DFT-computed ΔG of these steps. For the two O_2 dissociation steps, we compute only the rigid ligand dissociation energy, ΔE_{LD}, of O_2, which provides an upper bound on the energetics of O_2 dissociation. In addition to BEP relations, Marcus theory[105] suggests that the kinetics of electron transfer processes should be related to vertical ionization potential, ΔE_{IP} (Supporting Information Table S9 and Text S3). We thus also compute the ΔE_{IP} for both electron transfer steps, bringing the total to seven DFT properties that could capture catalytic activity (Supporting Information Table S10).

3b. Identifying Scaling Relationships for Similar WOCs.

Different electron configurations in molecular WOCs should influence their catalytic activity[106], limiting the understanding of differences in activity from geometric structure and chemical composition alone. To detect distinct electron configurations among the catalysts in our data set, we quantified differences based on the population of localized natural-bonding orbitals (NBOs, see Computational Details). Using the closed shell singlet Ru(II)-OH_2 intermediate, we collected the occupations of orbitals that localized to the $4s$ and $4d$ subshells of Ru(II) (i.e., six orbitals) or to the $2s$ and $2p$ subshells of the axial-coordinating O atom (i.e., four orbitals) into a 10-dimensional feature vector. Visualization of the first two principal components (95% of the variance) from principal component analysis (PCA) indicates that the 19 TMCs cluster into three distinct groups, with the largest group containing most (i.e., 15) TMCs (Figure 3 and Supporting Information Figure S3). These three groups are consistently present even if alternate intermediates are chosen for analysis (Supporting Information Figure S4).
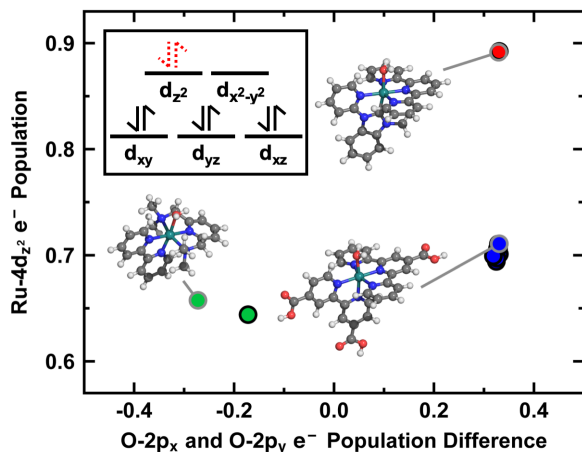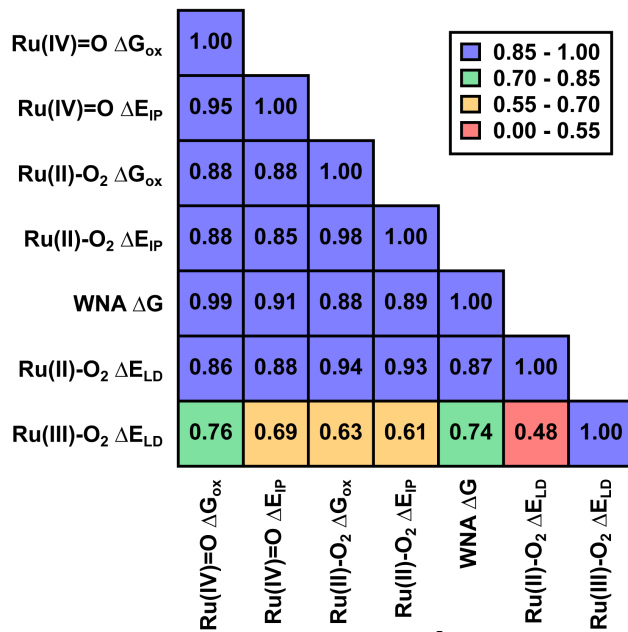
Figure 3. Plot of the natural orbital populations that distinguish electronic states the 19 TMCs studied: difference between the O $2p_x$ and $2p_y$ orbital populations vs Ru d_z^2 orbital total population. Fifteen catalysts (blue circles) have the qualitatively same populations, and two smaller clusters have enhanced d_z^2 populations (red) or distinct relative occupation in the p orbitals (green). Insets illustrate representative structures, and an electron configuration diagram provides a cartoon of the formal electron configuration (black solid arrows) and the additional density in the d_z^2 orbital for catalysts in the red cluster (red dashed arrows).

Relative to the majority cluster, the differences in the two outlier clusters can largely be attributed to either the Ru $4d_z^2$ or O $2p_x/2p_y$ orbitals, as the occupations of the remaining seven orbitals are nearly constant (Figure 3 and Supporting Information Table S11). Specifically, one cluster has additional electron density (ca. 0.2 e⁻) in the Ru $4d_{z^2}$ orbital, whereas electron density (ca. 0.3 e⁻) shifts from the oxygen $2p_x$ to the $2p_y$ orbital in the other cluster (Supporting Information Table S11). For the more oxidized intermediates (i.e. Ru(III)-OH, Ru(IV/V)=O, and Ru(III)-OOH), there is naturally less distinction between this second group and the 15-TMC majority group (Supporting Information Figure S4).

Since most TMCs in this work have similar electronic states, we focus our analysis of the relationship between DFT and experimental properties to this subset. For these 15 TMCs, most of the DFT properties are well correlated ($R^2 > 0.85$) with each other, indicating a single scaling relationship applies for all properties (Figure 4). The four electron transfer properties correlate positively to each other but negatively to the ΔG of the O-O bond formation step and ΔE_{LD} for

11

Ru(II)-O_2 (Supporting Information Figure S5). The single uncorrelated property, ΔE_{LD} of O_2 from Ru(III), does not correlate well with other steps in part because it is uniformly small (ca. 6 kcal/mol) for all catalysts in our data set (Figure 4 and Table S10). Since Ru(III)-O_2 ΔE_{LD} is an upper limit for ligand dissociation, we conclude it is unlikely to be rate limiting over these 15 TMCs and exclude it from further consideration.

	Ru(IV)=O ΔG_{ox}	Ru(IV)=O ΔE_{IP}	Ru(II)-O_2 ΔG_{ox}	Ru(II)-O_2 ΔE_{IP}	WNA ΔG	Ru(II)-O_2 ΔE_{LD}	Ru(III)-O_2 ΔE_{LD}
Ru(IV)=O ΔG_{ox}	1.00						
Ru(IV)=O ΔE_{IP}	0.95	1.00					
Ru(II)-O_2 ΔG_{ox}	0.88	0.88	1.00				
Ru(II)-O_2 ΔE_{IP}	0.88	0.85	0.98	1.00			
WNA ΔG	0.99	0.91	0.88	0.89	1.00		
Ru(II)-O_2 ΔE_{LD}	0.86	0.88	0.94	0.93	0.87	1.00	
Ru(III)-O_2 ΔE_{LD}	0.76	0.69	0.63	0.61	0.74	0.48	1.00

Legend:
- 0.85 - 1.00
- 0.70 - 0.85
- 0.55 - 0.70
- 0.00 - 0.55

Figure 4. Pearson correlation (R^2) between seven pairs of parameters calculated using DFT that might be expected to influence catalytic activity. Six of the parameters are well correlated to each other (blue, $R^2 > 0.85$), as indicated by the numerical values and colors in the inset legend.

Overall, most correlations are intuitive, e.g., a higher Ru(IV)=O ΔE_{IP} corresponds to more favorable WNA, whereas others, e.g., the negative correlation between ΔE_{IP} and ΔE_{LD} in Ru(II)-O_2, are less obvious (Supporting Information Table S12). While such correlations may not hold across a broader set that has greater structural or chemical diversity, they suggest consistent reactivity trends should be observable over the 15 TMC subset of molecular WOCs obtained from the three distinct experimental data sets. Overall, this analysis suggests a single scaling parameter can be used to estimate relative catalyst activity from DFT. We select Ru(II)-O_2 ΔE_{IP} as this scaling parameter since it has the largest average correlation (R^2: 0.86) and requires only a

single geometry optimization to compute (Figure 4).

3c. Thermodynamic Properties Predict Activity.

Since we have shown that the seven DFT properties which we expect to influence catalytic activity are correlated to each other, we next aim to determine if our chosen scaling parameter also correlates to experimentally-measured rate constants. For the 15 TMC subset, rate constants predicted based on a best-fit-line with the B3LYP Ru(II)-O_2 ΔE_{IP} match experimental rates to within a factor of three in all cases (Figure 5 and Supporting Information Tables S13–S14). This good performance (i.e., beyond typical hybrid DFT accuracy) is due to error cancellation possible only because we have curated a set of catalysts with comparable geometry and confirmed their comparable electronic structure with population-based analysis. TMC **7a** in experimental data set 1 is the only outlier in this analysis, with first-order dependence on oxidant concentration in its rate law whereas all other catalysts in this subset are zero-order in oxidant, preventing direct comparison to our descriptor on an equal footing (Figure 5). This is somewhat expected, as the 1.78 eV value of the Ru(II)-O_2 ΔE_{IP} descriptor for this catalyst is below the range of values (1.96–2.22 eV) for the other 14 TMCs from the majority cluster (Supporting Information Tables S10–S11). For large changes in the descriptor such as this, we expect commensurate changes to the rate of underlying elementary steps, potentially influencing which step is rate limiting. This observation highlights limitations of our single-descriptor approach, which may work best across subsets of catalysts where the rate-limiting step is unchanged.
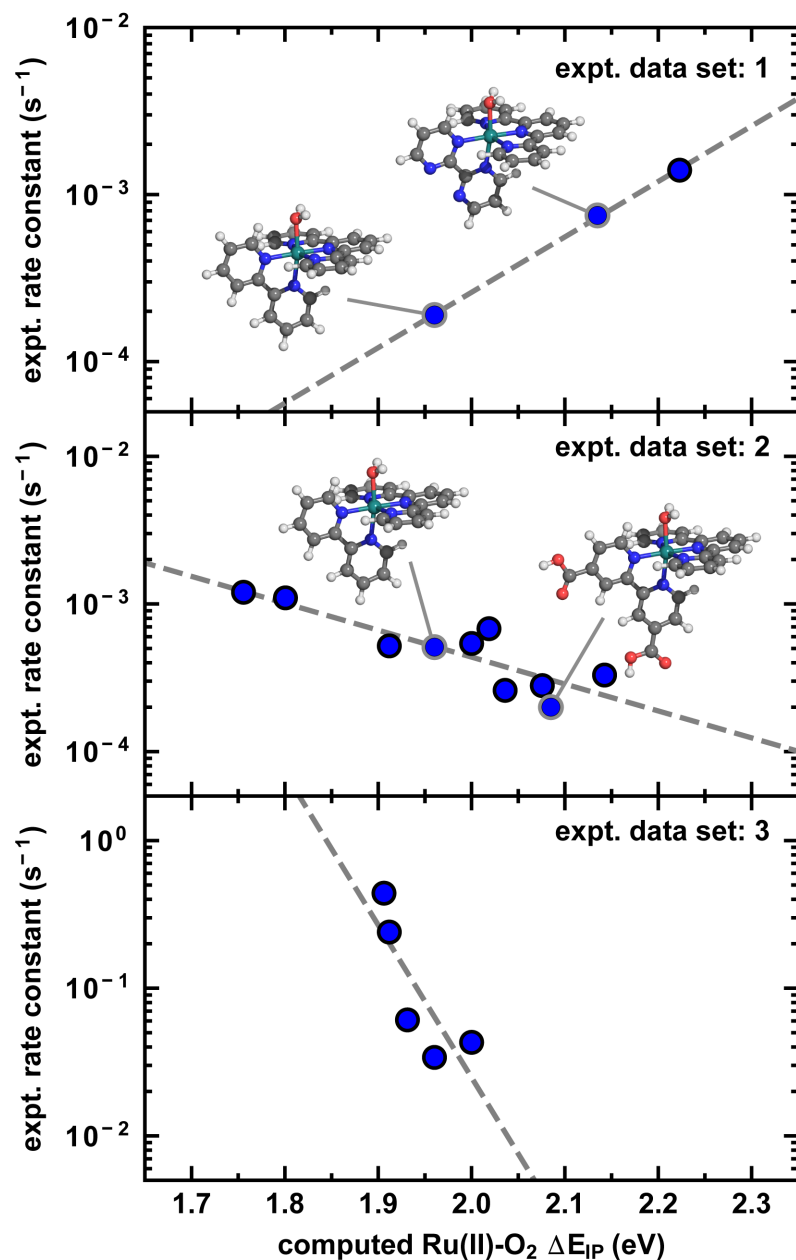
Figure 5. The experimentally measured rate constant (s^{-1}) vs the computationally-derived scaling parameter, Ru(II)-O_2 ΔE_{IP}, (in eV). The data is separated based on the reference of the experimental data, as indicated in the inset label in each pane. The Ru(II)-OH_2 intermediates of the **1a** and **1b** TMCs are shown as insets in data set 1, and **1a** and **1i** are shown as insets in data set 2 in ball and stick representation colored as: C in gray, O in red, N in blue, H in white, and Ru in teal. One data set 1 catalyst (**7a**) has a second order rate law and thus the rate constant cannot be visualized on this plot.

When identifying correlations between our descriptors and the experimental data sets, a

distinct best-fit line was observed for each set of experimental conditions (Figure 5). Thus, we

14

can use the slope of the correlation between our descriptor and experimentally measured rate constant to interpret possible differences in rate limiting steps with a change in experimental conditions. Based on this analysis, we conclude that the rate limiting step in data set 1 is either a ligand dissociation step or O-O bond formation, both of which become more energetically favorable as our descriptor increases (Supporting Information Table S12). In stopped flow cytometry experiments, ligand dissociation was assigned as the rate limiting step for these catalysts, consistent with our observation.[20] Conversely, in experimental data sets 2 and 3, one of the electron transfer steps could be rate limiting, as these become more favorable as the descriptor decreases (Supporting Information Table S12). We hypothesize these differences in rate limiting steps derive from differences in reaction conditions across experiments. For example, the concentration of oxidant (Ce^{IV}) was 30 equivalents in experimental data set 1 and excess in data sets 2 and 3.[8, 12-14] This additional oxidant potentially activates path two for O_2 release, enabling the catalyst to circumvent slower O_2 dissociation from Ru(II)-O_2.

We can understand the effect of changes in rate limiting steps on trends in catalytic activity by examining two additional representative TMCs (i.e., **1b** and **1i** along with **1a**). Both are differentiated from **1a** by the addition of peripheral electron-withdrawing groups that increase (by 0.12–0.17 eV) the Ru(II)-O_2 ΔE_{IP} scaling parameter (Figure 5). In data set 1, this modification (i.e., **1a** to **1b**) increases catalytic activity by nearly threefold (295%) due to more favorable dissociation of dioxygen from Ru(II)-O_2. In data set 2, the similar modification (i.e., **1a** to **1i**) decreases catalytic activity (by 61%) due to the decreasing favorability of electron transfer steps (Supporting Information Table S13). Therefore, we conclude that modifications to the catalyst that would result in an increase under one set of reaction conditions lead to diminished activity under differing reaction conditions.

**3d. Understanding the Activity of Dissimilar WOCs.**

In comparison to the 15 TMCs with similar electronic structure, there is experimental evidence[8] the other four catalysts have distinct rate limiting steps. Instead of zero-order dependence on the oxidant concentration as observed previously, experimental rates for three out of four remaining TMCs are first-order in oxidant. The rate order of the fourth TMC, **1f**, can be either zero- or first-order in oxidant depending on the progress of the reaction (Supporting Information Table S1). While the experimental rate appeared correlated to properties relevant to O_2 dissociation or O-O bond formation for the other catalysts from data set 1 (see Sec. 3c), the dependence of the rate on oxidant concentration suggests that the slowest step may involve electron transfer for these outlier TMCs. While we already noted that changes to the Ru(II)-O_2 ΔE_{IP} descriptor range (1.39-1.89 eV) in comparison to the majority TMCs (1.96-2.22 eV) can influence the rate law, this analysis suggests that changing the catalyst's preferred electronic state can also alter the slowest step in the catalytic cycle.

Unsurprisingly, the developed scaling relationship that applied to the 15 TMCs does not simultaneously apply to the four outlier TMCs (Supporting Information Figure S6). While for the 15 TMCs, deviations from scaling relations of energetic properties were small (ca. 0.5 kcal/mol), large deviations (ca. 4 kcal/mol) are observed when predicting the O-O bond formation and O_2 dissociation (i.e., WNA ΔG and Ru(II)-O_2 ΔE_{LD}) energetics of the outlier TMCs. Intermediate deviations (ca. 2 kcal/mol) are observed for prediction of the electron transfer steps (e.g., Ru(IV)=O ΔE_{IP}) for these four catalysts (Supporting Information Table S15). While the Ru(II)-O_2 ΔE_{IP} scaling parameter explains relative catalyst performance among 15 TMCs with similar electronic states in similar experimental conditions, it does not generalize across multiple electron configurations. Further, while additional scaling relations could be built for these outlier

catalysts, it would likely require more data (i.e., more than four catalysts) than is available from these three experimental sets.

Since quantitative analysis of the outlier catalysts is challenged by differences in rate order and scaling relations, we instead carry out a qualitative assessment. We focus on the Ru(II)-O_2 ΔE_{IP} vs. Ru(II)-O_2 ΔE_{LD} scaling relationship that applies to the 15 TMCs for the majority cluster but from which the outlier TMCs deviate strongly (Figure 6 and Supporting Information Figure S6). For the TMCs with increased $4d_z^2$ orbital occupation (i.e., **1d** and **1e**), Ru(II)-O_2 ΔE_{LD} values are lower (ca. 7 kcal/mol) than expected from the scaling relationship, suggesting more rapid O_2 dissociation (Figure 6 and Supporting Information Table S15). Since this deviation suggests more rapid O_2 dissociation, we would expect increased catalytic activity and rate-limiting electron transfer. Consistent with our expectations, **1d** and **1e** were approximately two orders of magnitude more active than **1a** in the original experimental study.[8] The decreased Ru(II)-O_2 ΔE_{LD} in **1d** and **1e** is likely due to the strong σ-donor ligand that can be expected to reduce the barrier to O_2 dissociation via the trans effect (Figure 1).
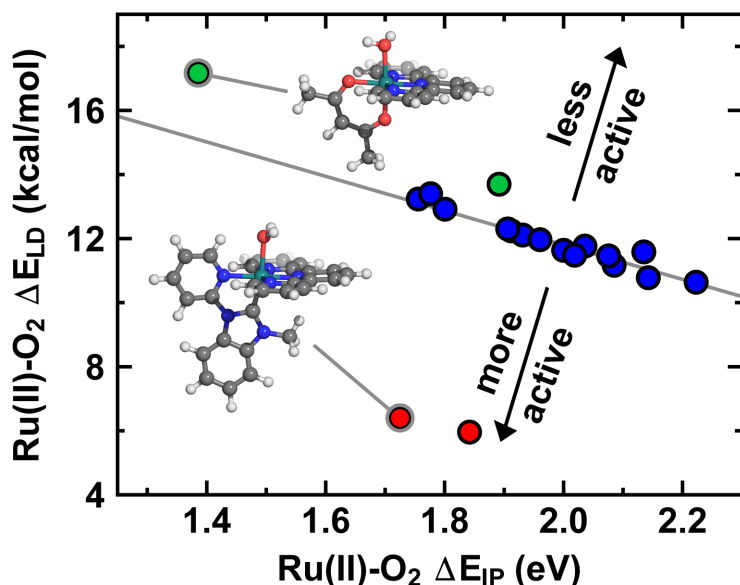

Figure 6. Ru(II)-O_2 ΔE_{IP} (in eV) vs. Ru(II)-O_2 ΔE_{LD} (in kcal/mol) for a majority cluster of 15 TMCs (blue circles) through which a best fit line (gray) is shown. Four TMCs excluded from the

fit are colored according to whether they have an increase in Ru d_z^2 occupation (red circles) or shifted relative O $2p_x$ and $2p_y$ occupations (green circles). Representative Ru(II)-OH$_2$ intermediates of inset TMCs are shown in ball and stick colored by element as: carbon in gray, nitrogen in blue, hydrogen in white, oxygen in red, and ruthenium in teal.

For the other two catalysts with shifted O $2p_x$ and $2p_y$ occupations (i.e., **1f** and **8a**), Ru(II)-O$_2$ ΔE_{LD} is instead increased (ca. 2 kcal/mol) relative to the scaling relationship (Figure 6, Supporting Information Table S15). Although this analysis might lead us to conclude that these two catalysts should undergo slower O$_2$ dissociation and have lower overall catalytic activity, experiments suggest they are both two orders of magnitude more active than **1a**.[8] This discrepancy can be rationalized by noting multiple paths for oxygen dissociation are possible in the WNA mechanism (Scheme 1). Since O$_2$ dissociation from Ru(II)-O$_2$ is somewhat less favorable for these TMCs without a decrease in activity, O$_2$ dissociation from Ru(III)-O$_2$ could instead be favored.

3e. Ligand Rigidity Improves Catalytic Activity.

Since all of the experimental WOCs studied in this work contain rigid multidentate ligands common among homogeneous Ru WOCs, we investigate the relative effect of lifting such constraints on catalyst energetics. By constructing lower denticity, monodentate analogues of the ligands in the multidentate **1a** WOC, we isolate the effect of conformational flexibility on changes in catalyst energetics (Figure 7 and Supporting Information Table S16). First, we note that both standard **1a** and its unconstrained form have fairly consistent reaction energetics (i.e., within 0.2 eV) for all but one step. The only exception is the oxidation of Ru(IV)=O to form Ru(V)=O, which is less favorable in the unconstrained TMC by 0.53 eV, suggesting rigidity is essential for stabilizing Ru(V)=O in TMC **1a**.
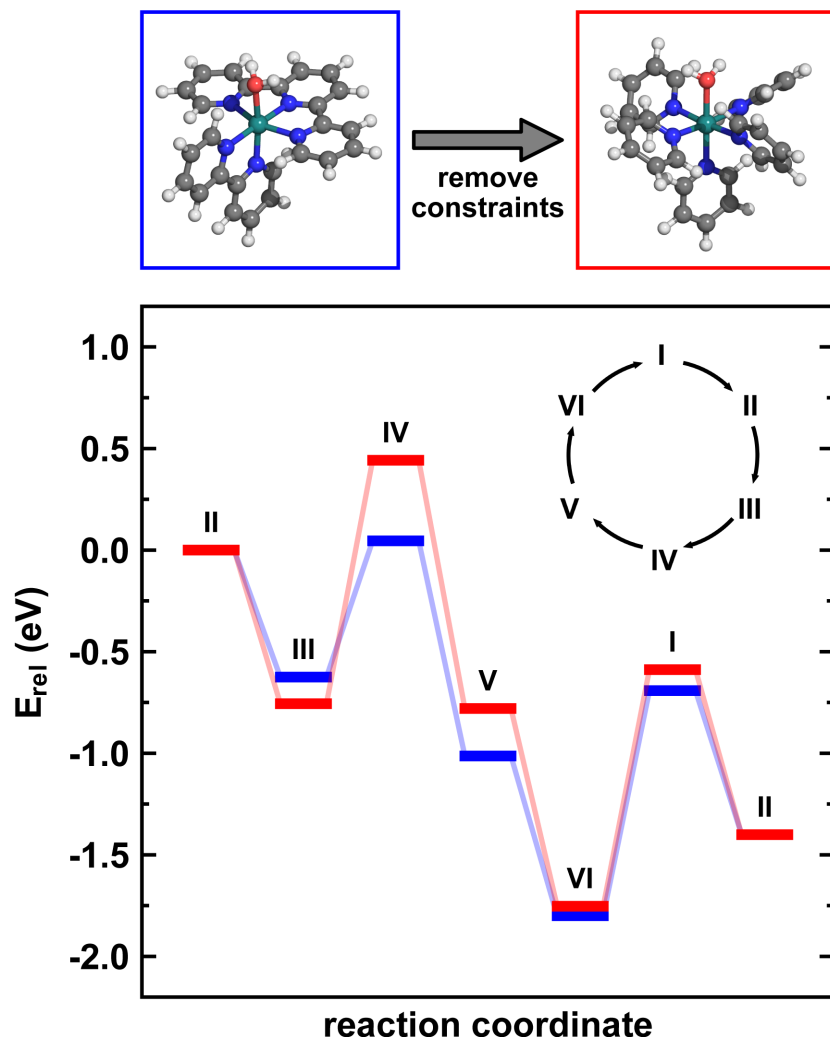
Figure 7. Comparison of energetics of the WNA catalytic cycle (in eV) when the TMC ligands are either conformationally constrained (blue) or unconstrained (red). Inset structures (top) show the bonds that are removed to construct an unconstrainted equivalent. Each step is identified as an intermediate labeled between I and VI, with the labels matching the intermediates in Scheme 1.

Given the emerging relevance of N-doped graphene single atom catalysts (SACs)[58] as a heterogeneous analogue to molecular catalysts for oxidation[36], we also investigated whether rigidity plays a role in the increased activity of SACs. We constructed a minimal SAC model consisting of Ru in a planar tetradentate structure reminiscent of an N-doped graphene sheet with a distal axial water as well as a monodentate, unconstrained form of the SAC model (Supporting Information Figure S7 and Table S16). When the denticity is reduced in the flexible model, we

19

observe a similar shift (by 0.52 eV) upward of the energetics for Ru(IV)=O oxidation to form Ru(V)=O, suggesting the effect of rigidity is indeed general (Supporting Information Table S17). Thus, we expect that rigidity in homogeneous WOCs or graphitic SACs will play a key role in stabilizing the key Ru(V)=O intermediate for the WNA mechanism to lead directly to O-O bond formation.

To predict the activity of the graphene SAC for water oxidation, we also compare to those of the 15 experimental TMCs. For five of the seven properties we identified to influence catalytic activity, the SAC model properties reside within the range of values obtained on the 15 TMCs (Supporting Information Tables S10 and S16). For the other two properties, i.e., ΔE_{LD} and ΔE_{IP} of the Ru(II)-O$_2$ intermediate, the SAC properties are significantly less favorable. The ΔE_{LD} of 20 kcal/mol is significantly higher (10–13 kcal/mol in the 15 TMCs) and the Ru(II)-O$_2$ ΔE_{IP} of 2.5 eV is also increased (1.8–2.2 eV in the 15 TMCs). These observations suggest that this SAC model is unlikely to efficiently catalyze a WNA mechanism because it disfavors both O$_2$ dissociation from Ru(II)-O$_2$ and formation of an Ru(III)-O$_2$ intermediate. Rather, SAC activity for water oxidation using Ru[107] or other metals[108-111] is likely the result of a modified mechanism involving an additional oxygen atom[107] or components of the extended SAC material that have an influence beyond rigidity alone.

4. Conclusions.

Small changes in catalyst structure and reaction conditions can lead to significant changes in catalytic rates in a manner that is challenging to predict from first principles. We demonstrated an alternate approach to building scaling relationships between efficiently computed first-principles (i.e., with DFT) properties and experimentally-measured rates across three studies of water oxidation catalysts. First, using a representative WOC, we identified the five most likely

rate-limiting steps in the WNA catalytic cycle. Then we computed seven cheap-to-calculate properties with DFT and observed six of the seven properties to correlate both to each other and the thermodynamics for each of the five key steps in WNA. From the relative activity of 19 experimentally-characterized WOCs from three different experimental studies reported in literature, we identified the ionization potential of a Ru(II)-O$_2$ intermediate to correlate well to the majority of catalyst activities across these experimental studies.

To explain when first-principles computed properties could not be correlated to experimental observations, we devised an approach to distinguishing the electronic state favored by the catalyst. Our metric for distinguishing electronic states among these catalysts depended on the electron population in the natural bonding orbitals of the metal center and axial oxygen atom. Using this metric, we confirmed that 15 of the TMCs had similar electron configurations for the Ru(II)-OH$_2$ intermediate, whereas two TMCs had increased electron density in the $4d_z{}^2$ orbital of the ruthenium center and two TMCs had electron density shifted from the $2p_x$ to the $2p_y$ orbital of oxygen. Across the studies where correlations could be obtained between experiment and computed properties, the slope of the correlation could be used to infer whether the experimental rate-limiting step of the reaction was O$_2$ dissociation, O-O bond formation, or electron transfer.

While scaling relationships do not easily generalize quantitatively to WOCs with distinct electronic states, qualitative inferences about the activity of possible TMCs were possible based on the sign of deviations from the scaling relationships. These observations motivated predictions of the role of rigidity in a Ru complex with more flexible ligands and a Ru SAC analogue. This approach reveals properties that govern the activity of homogeneous WOCs and provides a route toward computational design of improved catalysts for water oxidation.

ASSOCIATED CONTENT

Supporting Information. Tabulated values for the previously reported rate constants for catalysts in this work; details regarding spin states considered and energetic comparison between spin states; description of structure generation scheme; metrics for verifying octahedral geometry in optimized structures; a complete list of calculations which were excluded from analysis; procedure for recovery of calculations which initially did not converge to the intended result; description of calculations using functionals other than b3lyp and comparison of their results to the results of b3lyp; mathematical formulas for the calculation of each property in this work;, tabulated values for the ΔE_{vib} - TΔS correction for ΔG properties; reorganization energies associated with each electron transfer step for which we consider vertical ionization potential; derivation of the expected linear relationship between vertical ionization potential and reaction rate using Marcus theory; tabulated values for each of the seven DFT properties considered in depth in this work; PCA of electron density in valence orbitals of Ru(II)-OH$_2$ and other intermediates; tabulated values for the electron density in valence orbitals of Ru(II)-OH$_2$; scatter plots and equations for linear fits of the observed correlation between DFT properties; comparison of the reported rate constants and rate constants derived from our scaling relationships; scatter plots and tabulated values for the deviation from scaling relationships in catalysts with diverse electron structure; properties for **1a** and the graphene analogue with an without conformational constraints (PDF)

Structure files for the optimized geometries of all species considered in this work which pass our geometric and spin contamination criteria; complete list of calculations excluded from analysis due to non-octahedral geometries, spin contamination, or convergence issues; energies for all successful geometry optimizations and single point calculations in this work (ZIP)

AUTHOR INFORMATION

Corresponding Author

*email: hjkulik@mit.edu phone: 617-253-4584

Notes

The authors declare no competing financial interest.

References
1.	Lewis, N. S. Research Opportunities to Advance Solar Energy Utilization. *Science* **2016,** *351*, aad1920.
2.	Janet, J. P.; Ramesh, S.; Duan, C.; Kulik, H. J. Accurate Multiobjective Design in a Space of Millions of Transition Metal Complexes with Neural-Network-Driven Efficient Global Optimization. *ACS Cent. Sci.* **2020,** *6*, 513-524.
3.	Janet, J. P.; Duan, C.; Nandy, A.; Liu, F.; Kulik, H. J. Navigating Transition-Metal Chemical Space: Artificial Intelligence for First-Principles Design. *Acc. Chem. Res.* **2021,** *54*, 532-545.
4.	Janet, J. P.; Chan, L.; Kulik, H. J. Accelerating Chemical Discovery with Machine Learning: Simulated Evolution of Spin Crossover Complexes with an Artificial Neural Network. *J. Phys. Chem. Lett.* **2018,** *9*, 1064-1071.
5.	Concepcion, J. J.; Jurss, J. W.; Templeton, J. L.; Meyer, T. J. One Site Is Enough. Catalytic Water Oxidation by [Ru(Tpy)Bpm)(Oh$_2$)]$^{2+}$ and [Ru(Tpy)(Bpz)(Oh$_2$)]$^{2+}$. *J. Am. Chem. Soc.* **2008,** *130*, 16462-16463.
6.	Zong, R.; Thummel, R. P. A New Family of Ru Complexes for Water Oxidation. *J. Am. Chem. Soc.* **2005,** *127*, 12802-12803.
7.	Tseng, H.-W.; Zong, R.; Muckerman, J. T.; Thummel, R. Mononuclear Ruthenium(II) Complexes That Catalyze Water Oxidation. *Inorg. Chem.* **2008,** *47*, 11763-11773.
8.	Concepcion, J. J.; Jurss, J. W.; Norris, M. R.; Chen, Z.; Templeton, J. L.; Meyer, T. J. Catalytic Water Oxidation by Single-Site Ruthenium Catalysts. *Inorg. Chem.* **2010,** *49*, 1277-1279.
9.	Yoshida, M.; Masaoka, S.; Sakai, K. Oxygen Evolution from Water Catalyzed by Mononuclear Ruthenium Complexes with a Triazamacrocyclic Ligand in a Facial Fashion. *Chem. Lett.* **2009,** *38*, 702-703.
10.	Maji, S.; López, I.; Bozoglian, F.; Benet-Buchholz, J.; Llobet, A. Mononuclear Ruthenium–Water Oxidation Catalysts: Discerning between Electronic and Hydrogen-Bonding Effects. *Inorg. Chem.* **2013,** *52*, 3591-3593.
11.	Hoque, M. A.; Chowdhury, A. D.; Maji, S.; Benet-Buchholz, J.; Ertem, M. Z.; Gimbert-Suriñach, C.; Lahiri, G. K.; Llobet, A. Synthesis, Characterization, and Water Oxidation Activity of Isomeric Ru Complexes. *Inorg. Chem.* **2021,** *60*, 5791-5803.
12.	Wasylenko, D. J.; Ganesamoorthy, C.; Koivisto, B. D.; Henderson, M. A.; Berlinguette, C. P. Insight into Water Oxidation by Mononuclear Polypyridyl Ru Catalysts. *Inorg. Chem.* **2010,** *49*, 2202-2209.

13.   Yagi, M.; Tajima, S.; Komi, M.; Yamazaki, H. Highly Active and Tunable Catalysts for O$_2$ Evolution from Water Based on Mononuclear Ruthenium(II) Monoaquo Complexes. *Dalton Trans.* **2011,** *40*, 3802-3804.

14.   Watabe, S.; Tanahashi, Y.; Hirahara, M.; Yamazaki, H.; Takahashi, K.; Mohamed, E. A.; Tsubonouchi, Y.; Zahran, Z. N.; Saito, K.; Yui, T. Critical Hammett Electron-Donating Ability of Substituent Groups for Efficient Water Oxidation Catalysis by Mononuclear Ruthenium Aquo Complexes. *Inorg. Chem.* **2019,** *58*, 12716-12723.

15.   Duan, L.; Bozoglian, F.; Mandal, S.; Stewart, B.; Privalov, T.; Llobet, A.; Sun, L. A Molecular Ruthenium Catalyst with Water-Oxidation Activity Comparable to That of Photosystem II. *Nat. Chem.* **2012,** *4*, 418-423.

16.   Matheu, R.; Ertem, M. Z.; Benet-Buchholz, J.; Coronado, E.; Batista, V. S.; Sala, X.; Llobet, A. Intramolecular Proton Transfer Boosts Water Oxidation Catalyzed by a Ru Complex. *J. Am. Chem. Soc.* **2015,** *137*, 10786-10795.

17.   Boyer, J. L.; Polyansky, D. E.; Szalda, D. J.; Zong, R.; Thummel, R. P.; Fujita, E. Effects of a Proximal Base on Water Oxidation and Proton Reduction Catalyzed by Geometric Isomers of [Ru(Tpy)(Pynap)(Oh$_2$)]$^{2+}$. *Angew. Chem., Int. Ed.* **2011,** *50*, 12600-12604.

18.   Jacobsen, G. M.; Yang, J. Y.; Twamley, B.; Wilson, A. D.; Bullock, R. M.; DuBois, M. R.; DuBois, D. L. Hydrogen Production Using Cobalt-Based Molecular Catalysts Containing a Proton Relay in the Second Coordination Sphere. *Energy Environ. Sci.* **2008,** *1*, 167-174.

19.   Kotyk, J. F. K.; Hanna, C. M.; Combs, R. L.; Ziller, J. W.; Yang, J. Y. Intramolecular Hydrogen-Bonding in a Cobalt Aqua Complex and Electrochemical Water Oxidation Activity. *Chem. Sci.* **2018,** *9*, 2750-2755.

20.   Concepcion, J. J.; Tsai, M.-K.; Muckerman, J. T.; Meyer, T. J. Mechanism of Water Oxidation by Single-Site Ruthenium Complex Catalysts. *J. Am. Chem. Soc.* **2010,** *132*, 1545-1557.

21.   Duan, L.; Araujo, C. M.; Ahlquist, M. S. G.; Sun, L. Highly Efficient and Robust Molecular Ruthenium Catalysts for Water Oxidation. *Proc. Natl. Acad. Sci.* **2012,** *109*, 15584-15588.

22.   Duan, L.; Fischer, A.; Xu, Y.; Sun, L. Isolated Seven-Coordinate Ru(IV) Dimer Complex with [Hohoh]$^-$ Bridging Ligand as an Intermediate for Catalytic Water Oxidation. *J. Am. Chem. Soc.* **2009,** *131*, 10397-10399.

23.   Zhang, B.; Sun, L. Ru-Bda: Unique Molecular Water-Oxidation Catalysts with Distortion Induced Open Site and Negatively Charged Ligands. *J. Am. Chem. Soc.* **2019,** *141*, 5565-5580.

24.   Silva, J. L.; Unger, I.; Matias, T. A.; Franco, L. R.; Damas, G.; Costa, L. T.; Toledo, K. C. F.; Rocha, T. C. R.; de Brito, A. N.; Saak, C.-M. X-Ray Photoelectron Fingerprints of High-Valence Ruthenium–Oxo Complexes Along the Oxidation Reaction Pathway in an Aqueous Environment. *J. Phys. Chem. Lett.* **2019,** *10*, 7636-7643.

25.   Polyansky, D. E.; Muckerman, J. T.; Rochford, J.; Zong, R.; Thummel, R. P.; Fujita, E. Water Oxidation by a Mononuclear Ruthenium Catalyst: Characterization of the Intermediates. *J. Am. Chem. Soc.* **2011,** *133*, 14649-14665.

26.   Pushkar, Y.; Moonshiram, D.; Purohit, V.; Yan, L.; Alperovich, I. Spectroscopic Analysis of Catalytic Water Oxidation by [Ru^{ii}(Bpy)(Tpy) H2O]$^{2+}$ Suggests That Ru(V)=O Is Not a Rate-Limiting Intermediate. *J. Am. Chem. Soc.* **2014,** *136*, 11938-11945.

27.   Vogiatzis, K. D.; Polynski, M. V.; Kirkland, J. K.; Townsend, J.; Hashemi, A.; Liu, C.; Pidko, E. A. Computational Approach to Molecular Catalysis by 3d Transition Metals: Challenges and Opportunities. *Chem. Rev.* **2018,** *119*, 2453-2523.

28.   Hughes, T. F.; Friesner, R. A. Systematic Investigation of the Catalytic Cycle of a Single Site Ruthenium Oxygen Evolving Complex Using Density Functional Theory. *J. Phys. Chem. B* **2011,** *115*, 9280-9289.

29.   Wang, L.-P.; Wu, Q.; Van Voorhis, T. Acid−Base Mechanism for Ruthenium Water Oxidation Catalysts. *Inorg. Chem.* **2010,** *49*, 4543-4553.

30.   Chen, Z.; Concepcion, J. J.; Hu, X.; Yang, W.; Hoertz, P. G.; Meyer, T. J. Concerted O Atom–Proton Transfer in the O—O Bond Forming Step in Water Oxidation. *Proc. Natl. Acad. Sci.* **2010,** *107*, 7225-7229.

31.   Vigara, L.; Ertem, M. Z.; Planas, N.; Bozoglian, F.; Leidel, N.; Dau, H.; Haumann, M.; Gagliardi, L.; Cramer, C. J.; Llobet, A. Experimental and Quantum Chemical Characterization of the Water Oxidation Cycle Catalysed by [Ru^{ii}(Damp)(Bpy)(H$_2$O)]$^{2+}$. *Chem. Sci.* **2012,** *3*, 2576-2586.

32.   Angeles-Boza, A. M.; Ertem, M. Z.; Sarma, R.; Ibanez, C. H.; Maji, S.; Llobet, A.; Cramer, C. J.; Roth, J. P. Competitive Oxygen-18 Kinetic Isotope Effects Expose O–O Bond Formation in Water Oxidation Catalysis by Monomeric and Dimeric Ruthenium Complexes. *Chem. Sci.* **2014,** *5*, 1141-1152.

33.   Lin, X.; Hu, X.; Concepcion, J. J.; Chen, Z.; Liu, S.; Meyer, T. J.; Yang, W. Theoretical Study of Catalytic Mechanism for Single-Site Water Oxidation Process. *Proc. Natl. Acad. Sci.* **2012,** *109*, 15669-15672.

34.   Hirahara, M.; Ertem, M. Z.; Komi, M.; Yamazaki, H.; Cramer, C. J.; Yagi, M. Mechanisms of Photoisomerization and Water-Oxidation Catalysis of Mononuclear Ruthenium(II) Monoaquo Complexes. *Inorg. Chem.* **2013,** *52*, 6354-6364.

35.   Raugei, S.; DuBois, D. L.; Rousseau, R.; Chen, S.; Ho, M.-H.; Bullock, R. M.; Dupuis, M. Toward Molecular Catalysts by Computer. *Acc. Chem. Res.* **2015,** *48*, 248-255.

36.   Xu, H.; Cheng, D.; Cao, D.; Zeng, X. C. A Universal Principle for a Rational Design of Single-Atom Electrocatalysts. *Nat. Catal.* **2018,** *1*, 339-348.

37.   Wasylenko, D. J.; Ganesamoorthy, C.; Henderson, M. A.; Koivisto, B. D.; Osthoff, H. D.; Berlinguette, C. P. Electronic Modification of the [Ru^{ii}(Tpy)(Bpy)(Oh$_2$)]$^{2+}$ Scaffold: Effects on Catalytic Water Oxidation. *J. Am. Chem. Soc.* **2010,** *132*, 16094-16106.

38.   Moonshiram, D.; Pineda-Galvan, Y.; Erdman, D.; Palenik, M.; Zong, R.; Thummel, R.; Pushkar, Y. Uncovering the Role of Oxygen Atom Transfer in Ru-Based Catalytic Water Oxidation. *J. Am. Chem. Soc.* **2016,** *138*, 15605-15616.

39.   Zhan, S.; Triviño, J.; Ahlquist, M. r. The Carboxylate Ligand as an Oxide Relay in Catalytic Water Oxidation. *J. Am. Chem. Soc.* **2019,** *141*, 10247-10252.

40.   Ertem, M. Z.; Concepcion, J. J. Oxygen Atom Transfer as an Alternative Pathway for Oxygen–Oxygen Bond Formation. *Inorg. Chem.* **2020,** *59*, 5966-5974.

41.   Govindarajan, N.; Tiwari, A.; Ensing, B.; Meijer, E. J. Impact of the Ligand Flexibility and Solvent on the O–O Bond Formation Step in a Highly Active Ruthenium Water Oxidation Catalyst. *Inorg. Chem.* **2018,** *57*, 13063-13066.

42.   Pidko, E. A. Toward the Balance between the Reductionist and Systems Approaches in Computational Catalysis: Model Versus Method Accuracy for the Description of Catalytic Systems. *ACS Catal.* **2017,** *7*, 4230-4234.

43.   Bergeler, M.; Simm, G. N.; Proppe, J.; Reiher, M. Heuristics-Guided Exploration of Reaction Mechanisms. *J. Chem. Theory Comput.* **2015,** *11*, 5712-5722.

44.	Kuliaev, P. O.; Pidko, E. A. Operando Modeling of Multicomponent Reactive Solutions in Homogeneous Catalysis: From Non‑Standard Free Energies to Reaction Network Control. *ChemCatChem* **2020,** *12*, 795.

45.	Ertem, M. Z.; Gagliardi, L.; Cramer, C. J. Quantum Chemical Characterization of the Mechanism of an Iron-Based Water Oxidation Catalyst. *Chem. Sci.* **2012,** *3*, 1293-1299.

46.	Gimbert-Suriñach, C.; Moonshiram, D.; Francàs, L.; Planas, N.; Bernales, V.; Bozoglian, F.; Guda, A.; Mognon, L.; López, I.; Hoque, M. A. Structural and Spectroscopic Characterization of Reaction Intermediates Involved in a Dinuclear Co–Hbpp Water Oxidation Catalyst. *J. Am. Chem. Soc.* **2016,** *138*, 15291-15294.

47.	Hu, S.; Xu, P.; Xu, R.-X.; Zheng, X. Unveiling the High Catalytic Activity of a Dinuclear Iron Complex for the Oxygen Evolution Reaction. *Inorg. Chem.* **2021,** *60*, 7297-7305.

48.	Besora, M.; Maseras, F. Microkinetic Modeling in Homogeneous Catalysis. *Wiley Interdiscip. Rev.: Comput. Mol. Sci.* **2018,** *8*, e1372.

49.	Mao, Z.; Campbell, C. T. Kinetic Isotope Effects: Interpretation and Prediction Using Degrees of Rate Control. *ACS Catal.* **2020,** *10*, 4181-4192.

50.	Stegelmann, C.; Andreasen, A.; Campbell, C. T. Degree of Rate Control: How Much the Energies of Intermediates and Transition States Control Rates. *J. Am. Chem. Soc.* **2009,** *131*, 8077-8082.

51.	Kozuch, S.; Martin, J. M. L. What Makes for a Bad Catalytic Cycle? A Theoretical Study on the Suzuki− Miyaura Reaction within the Energetic Span Model. *ACS Catal.* **2011,** *1*, 246-253.

52.	Kozuch, S.; Shaik, S. How to Conceptualize Catalytic Cycles? The Energetic Span Model. *Acc. Chem. Res.* **2011,** *44*, 101-110.

53.	Abild-Pedersen, F.; Greeley, J.; Studt, F.; Rossmeisl, J.; Munter, T. R.; Moses, P. G.; Skulason, E.; Bligaard, T.; Nørskov, J. K. Scaling Properties of Adsorption Energies for Hydrogen-Containing Molecules on Transition-Metal Surfaces. *Phys. Rev. Lett.* **2007,** *99*, 016105.

54.	Man, I. C.; Su, H. Y.; Calle‑Vallejo, F.; Hansen, H. A.; Martínez, J. I.; Inoglu, N. G.; Kitchin, J.; Jaramillo, T. F.; Nørskov, J. K.; Rossmeisl, J. Universality in Oxygen Evolution Electrocatalysis on Oxide Surfaces. *ChemCatChem* **2011,** *3*, 1159-1165.

55.	Nørskov, J. K.; Bligaard, T.; Rossmeisl, J.; Christensen, C. H. Towards the Computational Design of Solid Catalysts. *Nat. Chem.* **2009,** *1*, 37-46.

56.	Latimer, A. A.; Kulkarni, A. R.; Aljama, H.; Montoya, J. H.; Yoo, J. S.; Tsai, C.; Abild-Pedersen, F.; Studt, F.; Nørskov, J. K. Understanding Trends in C–H Bond Activation in Heterogeneous Catalysis. *Nat. Mater.* **2017,** *16*, 225-229.

57.	Liao, P.; Getman, R. B.; Snurr, R. Q. Optimizing Open Iron Sites in Metal–Organic Frameworks for Ethane Oxidation: A First-Principles Study. *ACS Appl. Mater. Interfaces* **2017,** *9*, 33484-33492.

58.	Yang, X.-F.; Wang, A.; Qiao, B.; Li, J.; Liu, J.; Zhang, T. Single-Atom Catalysts: A New Frontier in Heterogeneous Catalysis. *Acc. Chem. Res.* **2013,** *46*, 1740-1748.

59.	Flytzani-Stephanopoulos, M. Gold Atoms Stabilized on Various Supports Catalyze the Water–Gas Shift Reaction. *Acc. Chem. Res.* **2014,** *47*, 783-792.

60.	Wodrich, M. D.; Sawatlon, B.; Busch, M.; Corminboeuf, C. The Genesis of Molecular Volcano Plots. *Acc. Chem. Res.* **2021,** *54*, 1107-1117.

61.	Cordova, M.; Wodrich, M. D.; Meyer, B.; Sawatlon, B.; Corminboeuf, C. Data-Driven Advancement of Homogeneous Nickel Catalyst Activity for Aryl Ether Cleavage. *ACS Catal.* **2020,** *10*, 7021-7031.

62.	Busch, M.; Wodrich, M. D.; Corminboeuf, C. Linear Scaling Relationships and Volcano Plots in Homogeneous Catalysis–Revisiting the Suzuki Reaction. *Chem. Sci.* **2015,** *6*, 6754-6761.

63.	Deshpande, S.; Kitchin, J. R.; Viswanathan, V. Quantifying Uncertainty in Activity Volcano Relationships for Oxygen Reduction Reaction. *ACS Catal.* **2016,** *6*, 5251-5259.

64.	Mori-Sánchez, P.; Cohen, A. J.; Yang, W. Many-Electron Self-Interaction Error in Approximate Density Functionals. *J. Chem. Phys.* **2006,** *125*, 201102.

65.	Ruzsinszky, A.; Perdew, J. P.; Csonka, G. I.; Vydrov, O. A.; Scuseria, G. E. Density Functionals That Are One-and Two-Are Not Always Many-Electron Self-Interaction-Free, as Shown for H_2^+, He_2^+, LiH^+, and Ne_2^+. *J. Chem. Phys.* **2007,** *126*, 104102.

66.	Haunschild, R.; Henderson, T. M.; Jimenez-Hoyos, C. A.; Scuseria, G. E. Many-Electron Self-Interaction and Spin Polarization Errors in Local Hybrid Density Functionals. *J. Chem. Phys.* **2010,** *133*, 134116.

67.	Cohen, A. J.; Mori-Sánchez, P.; Yang, W. Insights into Current Limitations of Density Functional Theory. *Science* **2008,** *321*, 792-794.

68.	Schmidt, T.; Kümmel, S. One-and Many-Electron Self-Interaction Error in Local and Global Hybrid Functionals. *Phys. Rev. B* **2016,** *93*, 165120.

69.	Mori-Sánchez, P.; Cohen, A. J.; Yang, W. Localization and Delocalization Errors in Density Functional Theory and Implications for Band-Gap Prediction. *Phys. Rev. Lett.* **2008,** *100*, 146401.

70.	Kulik, H. J. Perspective: Treating Electron over-Delocalization with the DFT+U Method. *J. Chem. Phys.* **2015,** *142*, 240901.

71.	Cramer, C. J.; Truhlar, D. G. Density Functional Theory for Transition Metals and Transition Metal Chemistry. *Phys. Chem. Chem. Phys.* **2009,** *11*, 10757-10816.

72.	Craig, M.; Garcia-Melchor, M. High-Throughput Screening and Rational Design to Drive Discovery in Molecular Water Oxidation Catalysis. *ChemRxiv* **2021**.

73.	Craig, M. J.; Coulter, G.; Dolan, E.; Soriano-López, J.; Mates-Torres, E.; Schmitt, W.; García-Melchor, M. Universal Scaling Relations for the Rational Design of Molecular Water Oxidation Catalysts with near-Zero Overpotential. *Nat. Commun.* **2019,** *10*, 1-9.

74.	Gani, T. Z. H.; Kulik, H. J. Understanding and Breaking Scaling Relations in Single-Site Catalysis: Methane-to-Methanol Conversion by Fe(IV)=O. *ACS Catal.* **2018,** *8*, 975-986.

75.	Nandy, A.; Kulik, H. J. Why Conventional Design Rules for C-H Activation Fail for Open Shell Transition Metal Catalysts. *ACS Catal.* **2020,** *10*, 15033-15047.

76.	Nandy, A.; Zhu, J.; Janet, J. P.; Duan, C.; Getman, R. B.; Kulik, H. J. Machine Learning Accelerates the Discovery of Design Rules and Exceptions in Stable Metal- Oxo Intermediate Formation. *ACS Catal.* **2019,** *9*, 8243-8255.

77.	Andrikopoulos, P. C.; Michel, C.; Chouzier, S.; Sautet, P. In Silico Screening of Iron-Oxo Catalysts for CH Bond Cleavage. *ACS Catal.* **2015,** *5*, 2490-2499.

78.	Wodrich, M. D.; Busch, M.; Corminboeuf, C. Accessing and Predicting the Kinetic Profiles of Homogeneous Catalysts from Volcano Plots. *Chem. Sci.* **2016,** *7*, 5723-5735.

79.	Petachem http://www.petachem.com. (accessed October 27, 2019).

80. Ufimtsev, I. S.; Martinez, T. J. Quantum Chemistry on Graphical Processing Units. 3. Analytical Energy Gradients, Geometry Optimization, and First Principles Molecular Dynamics. *J. Chem. Theory Comput.* **2009,** *5*, 2619-2628.

81. Lee, C.; Yang, W.; Parr, R. G. Development of the Colle-Salvetti Correlation-Energy Formula into a Functional of the Electron Density. *Phys. Rev. B* **1988,** *37*, 785.

82. Becke, A. D. Density-Functional Thermochemistry. III. The Role of Exact Exchange. *J. Chem. Phys.* **1993,** *98*, 5648-5652.

83. Stephens, P. J.; Devlin, F. J.; Chabalowski, C. F.; Frisch, M. J. Ab Initio Calculation of Vibrational Absorption and Circular Dichroism Spectra Using Density Functional Force Fields. *J. Phys. Chem.* **1994,** *98*, 11623-11627.

84. Hay, P. J.; Wadt, W. R. Ab Initio Effective Core Potentials for Molecular Calculations. Potentials for the Transition Metal Atoms Sc to Hg. *J. Chem. Phys.* **1985,** *82*, 270-283.

85. Ditchfield, R.; Hehre, W. J.; Pople, J. A. Self-Consistent Molecular-Orbital Methods. IX. An Extended Gaussian-Type Basis for Molecular-Orbital Studies of Organic Molecules. *J. Chem. Phys.* **1971,** *54*, 724.

86. Lange, A. W.; Herbert, J. M. A Smooth, Nonsingular, and Faithful Discretization Scheme for Polarizable Continuum Models: The Switching/Gaussian Approach. *J. Chem. Phys.* **2010,** *133*, 244111.

87. York, D. M.; Karplus, M. A Smooth Solvation Potential Based on the Conductor-Like Screening Model. *J. Phys. Chem. A* **1999,** *103*, 11060-11079.

88. Liu, F.; Luehr, N.; Kulik, H. J.; Martínez, T. J. Quantum Chemistry for Solvated Molecules on Graphical Processing Units Using Polarizable Continuum Models. *J. Chem. Theory Comput.* **2015,** *11*, 3131-3144.

89. Liu, F.; Sanchez, D. M.; Kulik, H. J.; Martínez, T. J. Exploiting Graphical Processing Units to Enable Quantum Chemistry Calculation of Large Solvated Molecules with Conductor‐Like Polarizable Continuum Models. *Int. J. Quantum Chem.* **2019,** *119*, e25760.

90. Saunders, V. R.; Hillier, I. H. A "Level-Shifting" Method for Converging Closed Shell Hartree-Fock Wave Functions. *Int. J. Quantum Chem.* **1973,** *7*, 699-705.

91. Wang, L.-P.; Song, C. Geometry Optimization Made Simple with Translation and Rotation Coordinates. *J. Chem. Phys.* **2016,** *144*, 214108.

92. Ioannidis, E. I.; Gani, T. Z. H.; Kulik, H. J. molSimplify: A Toolkit for Automating Discovery in Inorganic Chemistry. *J. Comput. Chem.* **2016,** *37*, 2106-2117.

93. molSimplify Documentation. http://molsimplify.mit.edu (accessed March 3, 2021).

94. Group, K. molSimplify & molSimplify Automatic Design. https://github.com/hjkgrp/molsimplify (accessed March 3, 2021).

95. O'Boyle, N. M.; Banck, M.; James, C. A.; Morley, C.; Vandermeersch, T.; Hutchison, G. R. Open Babel: An Open Chemical Toolbox. *J. Cheminf.* **2011,** *3*, 33.

96. O'Boyle, N. M.; Morley, C.; Hutchison, G. R. Pybel: A Python Wrapper for the Open Babel Cheminformatics Toolkit. *Chem. Cent. J.* **2008,** *2*, 5.

97. Nandy, A.; Duan, C.; Janet, J. P.; Gugler, S.; Kulik, H. J. Strategies and Software for Machine Learning Accelerated Discovery in Transition Metal Chemistry. *Ind. Eng. Chem. Res.* **2018,** *57*, 13973-13986.

98. Yanai, T.; Tew, D. P.; Handy, N. C. A New Hybrid Exchange–Correlation Functional Using the Coulomb-Attenuating Method (Cam-B3LYP). *Chem. Phys. Lett.* **2004,** *393*, 51-57.

99. Chai, J.-D.; Head-Gordon, M. Systematic Optimization of Long-Range Corrected Hybrid Density Functionals. *J. Chem. Phys.* **2008,** *128*, 084106.

100.   Rohrdanz, M. A.; Martins, K. M.; Herbert, J. M. A Long-Range-Corrected Density Functional That Performs Well for Both Ground-State Properties and Time-Dependent Density Functional Theory Excitation Energies, Including Charge-Transfer Excited States. *J. Chem. Phys.* **2009,** *130,* 054112.

101.   Gagliardi, C. J.; Vannucci, A. K.; Concepcion, J. J.; Chen, Z.; Meyer, T. J. The Role of Proton Coupled Electron Transfer in Water Oxidation. *Energy Environ. Sci.* **2012,** *5,* 7704-7717.

102.   Fahmida, K.; Sonalika, A.; Ganesh, S. Reaction Mechanism of the Ceric Oxidation of Benzohydroxamic Acid with Different Acid Medium. *Res. J. Chem. Environ.* **2013,** *17,* 5.

103.   Bell, R. P. The Theory of Reactions Involving Proton Transfers. *Proc. R. Soc. London, Ser. A* **1936,** *154,* 414-429.

104.   Evans, M. G.; Polanyi, M. Inertia and Driving Force of Chemical Reactions. *Trans. Faraday Soc.* **1938,** *34,* 11-24.

105.   Marcus, R. A.; Sutin, N. Electron Transfers in Chemistry and Biology. *Biochim. Biophys. Acta, Rev. Bioenerg.* **1985,** *811,* 265-322.

106.   Betley, T. A.; Wu, Q.; Van Voorhis, T.; Nocera, D. G. Electronic Design Criteria for O−O Bond Formation via Metal−Oxo Complexes. *Inorg. Chem.* **2008,** *47,* 1849-1861.

107.   Cao, L.; Luo, Q.; Chen, J.; Wang, L.; Lin, Y.; Wang, H.; Liu, X.; Shen, X.; Zhang, W.; Liu, W. Dynamic Oxygen Adsorption on Single-Atomic Ruthenium Catalyst with High Performance for Acidic Oxygen Evolution Reaction. *Nat. Commun.* **2019,** *10,* 1-9.

108.   Zhang, L.; Jia, Y.; Gao, G.; Yan, X.; Chen, N.; Chen, J.; Soo, M. T.; Wood, B.; Yang, D.; Du, A. Graphene Defects Trap Atomic Ni Species for Hydrogen and Oxygen Evolution Reactions. *Chem* **2018,** *4,* 285-297.

109.   Guan, J.; Duan, Z.; Zhang, F.; Kelly, S. D.; Si, R.; Dupuis, M.; Huang, Q.; Chen, J. Q.; Tang, C.; Li, C. Water Oxidation on a Mononuclear Manganese Heterogeneous Catalyst. *Nat. Catal.* **2018,** *1,* 870-877.

110.   Zheng, Y.; Jiao, Y.; Zhu, Y.; Cai, Q.; Vasileff, A.; Li, L. H.; Han, Y.; Chen, Y.; Qiao, S.-Z. Molecule-Level G-C_3n_4 Coordinated Transition Metals as a New Class of Electrocatalysts for Oxygen Electrode Reactions. *J. Am. Chem. Soc.* **2017,** *139,* 3336-3339.

111.   Lee, W. H.; Ko, Y.-J.; Kim, J.-Y.; Min, B. K.; Hwang, Y. J.; Oh, H.-S. Single-Atom Catalysts for the Oxygen Evolution Reaction: Recent Developments and Future Perspectives. *Chem. Commun.* **2020,** *56,* 12687-12697.

For Table of Contents Only